Journal of
Materials Chemistry B

Materials for biology and medicine

Accepted Manuscript

This article can be cited before page numbers have been issued, to do this please use: K. Almpanidis, A. Panagiotopoulos, G. Kakavelakis, L. Askew, X. Pu, D. Kutsarov, S. Hinder, S. R. P. Silva and V. Stolojan, *J. Mater. Chem. B*, 2026, DOI: 10.1039/D5TB02697K.

ROYAL SOCIETY OF CHEMISTRY

rsc.li/materials-b

A Low-Cost Titanium Suboxide pH Sensor with Competitive Operational Lifetime Assessed with Electrochemical Impedance Spectroscopy

Kyriakos Almpanidis[a], Apostolos Panagiotopoulos[a], George Kakavelakis[b], Leslie Askew[a], Xiaoqian Pu[a], Dimitar I. Kutsarov[a], Steven J. Hinder[c], S. Ravi P. Silva[a,d] and Vlad Stolojan[a,d*]

[a] Advanced Technology Institute, School of Computer Science and Electronic Engineering, University of Surrey, Guildford, UK, GU2 7XH

[b] Department of Electronic Engineering, School of Engineering, Hellenic Mediterranean University, Romanou 3, Chalepa, Chania, Crete, Greece, 731 33

[c] Surface Analysis Laboratory, School of Mechanical Engineering Sciences, University of Surrey, Guildford, UK, GU2 7XH

[d] Institute for Sustainability, University of Surrey, Guildford, UK, GU2 7XH

[*] Corresponding author: v.stolojan@surrey.ac.uk

Keywords: pH sensors, Electrochemical Impedance Spectroscopy, Smart Bandages, Wound Monitoring, Transition Metal Oxides

Abstract

Smart Bandages are an emerging field of wearable electronics. Biosensors provide a medium of communication between the wound site's chemical status and the clinicians. The pH is a critical biomarker, as it is a suitable indicator for bacterial infection. In this paper, a low-cost Electrochemical Impedance Spectroscopy (EIS)-based Titanium Suboxide (TiO_x) pH sensor with Silver (Ag) electrodes is presented. A sensitivity of -27.8 Ω/pH is achieved in the pH 4-8 region of interest related to wound infection. The measured pH sensitivity, after a one-month stability study, is lost only 2.25% for the TiO_x sensor - reaching the state-of-the-art - compared to the Polyaniline (PANI) sensor, which lost 10% of its pH sensitivity. To further assess stability, we evaluated sensor behaviour at the edge pH values. The TiO_x sensor exhibits impedance increases of 5.5% and 4% at pH 4 and 8, respectively, which are approximately half of those reported for PANI devices (10% and 9% at pH 4 and 8, respectively). The stability experiments highlighted TiOx's chemical stability relative to PANI in both acidic and alkaline media. Further, the sensitivity of the TiO_x sensors is recovered to 95.7% after 200℃ thermal annealing, thereby recalibrating the sensors and prolonging their lifetime whilst reducing waste. To better understand the sensing and degradation mechanisms, a model-free method is employed for both TiO_x and PANI pH sensors. The reason is to demonstrate that pH sensitivity is related to the film surface (given the circuit complexity of the equivalent models in 2-electrode systems). This work is an important step for a potential translation to real-world wound monitoring, where long-term stability and low cost are critical for an accurate and efficient biomarker detection and sustainable well-being.

View Article Online
DOI: 10.1039/D5TB02697K

Introduction

Chronic wounds, defined by a failure to heal within 30 days[1, 2], represent a significant and growing healthcare challenge. Smart bandages have been proposed as a solution for monitoring chronic wounds[3, 4]. Their role is to track wound conditions and enable the early detection of infections and/or delayed healing, making them preferable to conventional bandages. These biomedical platforms contribute to the field of wearable electronics[5] by not only monitoring biomarkers (such as pH, temperature, glucose, etc.)[6] at the wound site, but also enabling on-demand therapeutics[7]. Specifically, a biosensor array is embedded to transduce data (such as the concentration of analytes and metabolites[8]) both with Faradaic (charge transfer) or non-Faradaic (adsorption)[9] chemiresistive approaches. These electrochemical phenomena are translated to the healthcare providers or users as voltage or current[10, 11] signals, while also possessing the capability to provide targeted drug delivery. Biosensors for biomarker monitoring, embedded in smart bandages, provide several benefits versus conventional bandages, such as a decrease in the number of wound dressing changes[4], reduced healthcare costs and hospitalisation time[12]. These benefits are critical for the long-term health and well-being, one of the Sustainable Development Goals adopted by the United Nations[13].

Among the monitored biomarkers, pH is important for chronic wound management because an alkaline pH is a key indicator of bacterial infection[14] at the wound surface. Also, an accurate pH measurement is essential for calibrating[15] other enzymatic biosensors (e.g., for glucose and lactate). Organic semiconductors like Polyaniline (PANI)[16] are widely used for pH sensing due to their high proton sensitivity[17]. However, PANI changes phase from Emeraldine salt to base, which leads to limited chemical stability[18] in aqueous environments. The tendency of organic semiconductors to oxidise[18] and swell[19] causes performance degradation over periods ranging from hours[20] up to 14 days[21-23]. These stability periods make organic semiconductors inadequate for chronic wound monitoring, which requires stability over several weeks to months. Therefore, an accurate aftercare cannot be accomplished, as it takes one month to determine whether a wound is chronic or not[1].

In contrast, transition metal oxides (TMOs) such as iridium suboxide (IrO_x[24-27]), molybdenum suboxide (MoO_x[28]), and titanium suboxide (TiO_x)[29, 30] have demonstrated a long-term chemical stability in emerging applications such as electrocatalysis[31, 32], memristors[33] and solar cells[34, 35]. However, the existing stability studies on pH sensors have demonstrated 2%-10%[23, 36-38] degradation, but with some caveats related to the testing stability protocol and the real-world

View Article Online
DOI: 10.1039/D5TB02697K

timeline for chronic wound monitoring (one-month lifetime). The reported stability tests are often too short (a few hours[36, 39] to two weeks[23]) or conducted at a single pH value (mostly around 7.4[23, 37], 8[36] or 5.5[38]). Also, studies involving high-temperature in situ processes (e.g., continuous heating of the substrate at 800°C for Al_2O_3[40]) are incompatible with flexible, wearable substrates and IoT applications. Furthermore, other studies report substantial losses in sensitivity (~20%[41]) or an increase (~50%[26]) in the response time after four weeks. Hence, in this work, we report a more extensive chemical stability study that monitors a pH sensor: a) at high and low pH values, b) sensitivity over one month and c) recovery after 3 months.

Most wearable pH sensors rely on potentiometric methods like Open Circuit Potential (OCP)[42], for detecting voltage changes for different pH solutions, which offers a non-invasive measurement (steady-state equilibrium, no current in the cell[43]). However, OCP provides limited insight into the interfacial kinetics at the electrode-electrolyte interface, which are related to the pH sensing (proton detection) mechanism[38, 44]. Electrochemical Impedance Spectroscopy (EIS)[45] is a powerful technique that characterises these interfacial processes—double-layer charging[46], charge-transfer resistance[47], ionic motion[48]—. EIS operates with a minimal signal perturbation by applying a small AC voltage (typically 10 mV) across a frequency spectrum (Hz to MHz)[49].

While EIS is typically performed using a three-electrode setup, working electrode (WE), Counter electrode (CE) and reference electrode (RE), a two-electrode system (WE, CE – such as in this paper, see Figure 1) is preferred for wearable applications due to its simplicity and necessity for RE's calibration. This calibration process requires care with electrolyte management, junction maintenance, and cleaning, which is largely incompatible with flexible smart bandage designs. Previous attempts at two-electrode impedimetric pH sensing, achieving sensitivities of some kΩ/pH[50-53] but have faced issues with structural stability (interdigitated electrodes structural instability after two weeks[51, 53]). Also, they have tested at a limited pH range (pH 6.5-7.5[51]), poor reproducibility (high impedance after 3-4 tests[52]), and a lack of validation regarding signal causality and selectivity. Moreover, a full frequency sweep requires complex hardware that increases the size and power consumption of a wearable device. Therefore, a pH sensor that leverages the analytical power of EIS while operating at a single optimal frequency would be advantageous. Single-frequency EIS provides an informative and accurate signal while minimising the hardware complexity.

View Article Online
DOI: 10.1039/D5TB02697K

Furthermore, advanced EIS data analysis techniques (except for the typical circuit equivalent fitting[54]), such as the Distribution of Relaxation Times (DRT)[55, 56], offer a model-free method to deconvolute contributing electrochemical processes. DRT can cross-validate sensing mechanisms, enhancing the reliability of the data interpretation. Also, DRT eliminates the bias that is typically introduced from circuit models that often cannot deconvolute processes with near-overlapping relaxation time values[57].

The electrode-conducting material is a key factor in electrochemical biosensors because it contributes significantly to the sensor's final cost. The current state-of-the-art for biosensors often relies on microfabricated electrodes made from noble metals such as gold (Au), platinum (Pt), palladium (Pd)[5, 15, 58]. Exploring alternative, low-cost materials such as silver (Ag)[59] or aluminium (Al)[52] for electrodes and TMOs (such as TiO_x) for sensing layers, that do not compromise the signal integrity, is necessary for sustainable and accessible wearable technology. The Ag can be fully recycled many times without any loss of quality[60] and many research works highlighted its longevity[61]. Hence, the environmental harm associated with its use can be reduced, while its circularity provides an opportunity to reuse Ag resources without extracting new minerals from the earth. On the other hand, TiO_x films (not nanoparticle form) are a well-known material for their longevity[62], and their water insolubility[62] minimises the risk of leakage into the sea and sewage water.

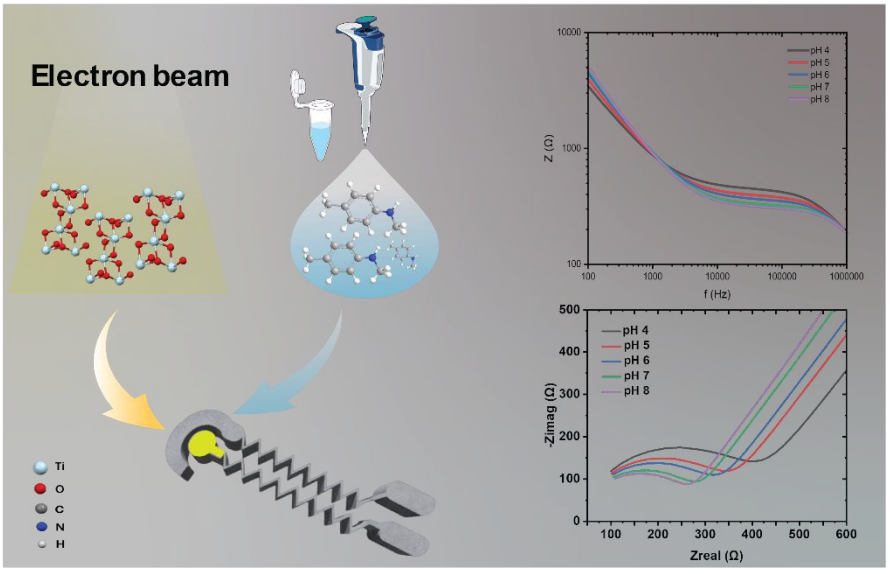

Figure 1. The sensor structure will be utilised in this paper. The TiO_x and PANI films were fabricated using e-beam and drop-casting, respectively. Concept: From pH concentration to a measurable electric signal (EIS signal, in this study).

The Ag can be a potential for integration to commercialised smart bandages, if the surface corrosion or any Ag^+ release to the wound can be minimised. In the literature, many biocompatible materials such as Nafion[63], PDMS, Parylene C[15, 64] and Ti alloys[65] have been

View Article Online
DOI: 10.1039/D5TB02697K

employed for encapsulation. Hence, both the sensor's environmental stability and the Ag+ release may be reduced. Furthermore, cytocompatibility tests such as MTT assay, in accordance with the ISO 10993-5, are employed to investigate any cytotoxicity from the Ag^+ release[66]. A careful experimental planning such as[67, 68]: a) washing cells with PBS and afterwards adding the fresh media with MTT to reduce the chemical interaction during the assay test, b) conduct control tests between cells, MTT and Ag^+ (in pairs) to subtract the background readings, and c) cross-validate the results with less Ag^+ sensitive assays, such as ATP-based assays can increase the reliability of the cytocompatibility results regarding the integration of Ag electrodes to smart bandages.

In this paper, a prototype single-frequency EIS pH sensor based on TiO_x as the pH-sensing material is presented, highlighting its greater time stability (31-day stability studies and impedance recovery after 3 months) compared with the state-of-the-art PANI, which is much more expensive than TiO_x. The effect of the pH on the electrochemical cell was quantified by measuring the cell's impedance in the 100 Hz - 1 MHz frequency range. The TiO_x pH sensor lost only 2.25% of its sensitivity for one month, compared to 10% observed for the reference PANI devices. Additionally, the TiO_x sensor's impedance increased 5.5% (pH 4) and 4% (pH 8), compared to 10% (pH 4) and 9% (pH 8) observed for the reference PANI pH sensors, showing TiO_x's superior interfacial chemical stability to both alkaline and acidic media. Furthermore, it was possible to regenerate the sensor's sensitivity by up to 95.6%, after a simple thermal annealing at 200℃ for 2 hours. Thermal annealing enhances the lifetime of the TiOx sensor and reduces waste. The sensing mechanism has also been examined, and the contribution of the TiO_x surface to pH sensing and degradation has been demonstrated. To further demonstrate the sensor's functionality, experiments have been conducted to highlight the reversibility and causality of the measuring signal, thereby enhancing its reliability. The results have also indicated a minimum Ag corrosion during the stability experiments, further highlighting the TiO_x sensor's potential for low-cost applications. Finally, the sensing and degradation mechanisms have also been studied using a model-free approach to cross-validate our results and further demonstrate the potential of low-cost TiO_x-based pH sensor platforms for real-world chronic wound monitoring, where long-term accuracy and robustness are critical.

Experimental

Materials

View Article Online
DOI: 10.1039/D5TB02697K

Silver wire was purchased from Goodfellows Advanced Materials in the UK. TiO_2 pellets from Testbourne Ltd, UK. PANI Emeraldine Base, HCl, acetone and isopropyl alcohol were purchased from Sigma Aldrich, UK. Si/SiO_2 wafers were purchased from Si-Mat Silicon Materials Technologies, Germany. LOR5A was purchased from Kayaki Advanced Materials, US. S1813. AZ726MIF and Hellmanex (TM) III were purchased from Merck, Germany. Microposit Remover 1165 (MR1165) was purchased from DuPont, US.

Fabrication of the Ag electrodes

Ag electrodes were fabricated using bi-layer lift-off photolithography. Si/SiO_2 (300 nm thermal growth) wafers were cleaned by dipping in 1% v/v Hellmanex solution in deionised water, acetone and isopropyl alcohol for 10 minutes each. Next, the wafers were dried using an N2 gun and O2 plasma-treated (Diener Zepto-BRs 200, 10 minutes, 200W). LOR5A was then spin-coated (Ems 6000 photoresist spinner) at 500 rpm for 15 sec, followed by 3500 rpm for 60 sec. A baking step on a hotplate (Stuart UC152D) was followed at 180℃ for 330 seconds. After cooling for 15 minutes to clean room temperature, a layer of S1813 positive photoresist was spin-coated (Ems 6000 photoresist spinner), using the same conditions as for LOR5A, and then baked (Ems 1000-1) at 115℃ for 15 minutes, and finally cooled down to clean room temperature for 15 minutes. The electrodes were patterned using a laser writer (Heidelberg Instruments Mikrotechnik GmbH CDL66+, 70 mW) and developed using AZ726MIF for 3 minutes. The wafer was inserted into an e-beam evaporator (Univex e-beam evaporator), and a thin film of Ti/Ag (15 nm/85 nm) was deposited at an evaporation rate of 0.2 Å/s whilst the wafer was rotated at 25 rpm. The film thickness was monitored in situ using a quartz-crystal microbalance sensor. The vacuum at the start of the evaporation process was $5 \cdot 10^{-7}$ Torr. After the evaporation finished, lift-off was completed by dipping the wafer into MR1156 remover at 65℃ for 3 hours.

TiO_x film deposition

The TiO_x film was deposited using e-beam evaporation (Univex e-beam evaporator) from the TiO_2 source (Figure 1). The evaporation rate was kept at 0.2 Å/s, and the wafer was rotated at 25 rpm. The vacuum at the start of the evaporation process was $6 \cdot 10^{-7}$ Torr. The TiO_x material was deposited only onto the working electrode area using laser-structured evaporation masks. For this purpose, a Kapton sheet with a thickness of 75 µm was placed on top of a vacuum table, and the required design was scribed with a picosecond laser for Coherent

View Article Online
DOI: 10.1039/D5TB02697K

(HyperRapid NXT). The lasing was carried out with a laser burst frequency and speed of 500 kHz and 500 mm/s, respectively. This resulted in a total power of 5.0 W cm^2.

PANI film deposition

PANI emeraldine base (PANI-EB) was dissolved in DMSO at 0.2%wt, similar to the method described in [59]. The solution was stirred overnight. Following that, it was doped in a 2% wt 0.02 M HCl solution to induce PANI emeraldine salt (PANI-ES) conductive species and stirred overnight. 1 μL of the final solution was drop-casted onto the WE (Figure 1), and an annealing step followed, at 60℃ for 2 hours.

Electrochemical characterisation

The pH sensors were tested using McIlvaine buffer solutions in the range 4-8 (each solution pH tested using a pH meter (Hannah Instruments Ltd.) and pH indicator strips (FisherBrand). PLA 3-D printed rings were placed onto the WE and CE area to keep the buffer solution in the WE-CE area. Using a micropipette, 33 μL of each buffer solution was placed onto the electrode area. EIS were obtained using Gamry1000, at 10 mV ac Voltage, 0 DC bias, and at frequencies from 100 Hz to 1 MHz with 10 points per decade and normal mode of denoising. Each measurement began after a 120-second open-circuit delay to allow system stabilisation. The pH sensors were connected to the Gamry1000 using test stand PCB spring-loaded clips. For the time stability, two different types of tests were performed: the first evaluates time stability by measuring the impedance at 100 kHz for pH 4 and pH 8 buffer solutions, for separate devices, and the second by measuring the sensitivity in the range pH 4-8, in a 31-day time window. The devices were kept in each experiment's pH conditions throughout the stability time. After every EIS measurement, the droplet was removed using absorbent wipes[69]. The buffer solutions were replaced and tested every 15 days.

Thermal annealing treatment

The thermal annealing treatment (for sensitivity recovery) was carried out using a Lenton Furnace (Lenton Laboratory & Scientific Equipment PTY (Ltd)). The plateau temperature was 200℃ for 2 hours, with a temperature increase rate of 1℃/min.

Kelvin Probe Measurements (KP)

Kelvin Probe measurements were performed in air (KPTechnology Ltd, version KP020). The work function (WF) of the sample is calculated by measuring the contact potential difference (CPD), using the formulas below:

$$\text{WF of the tip} = \text{WF of the test sample} - \text{CPD (test sample)}$$

$$\text{WF of the sample} = \text{WF of the tip} + \text{CPD (sample)}$$

The test sample is the highly ordered pyrolytic graphite (HOPG) with WF = 4.48 eV[70].

Ultraviolet-Visible (UV-Vis) – Absorption Spectroscopy

UV-Vis spectra (absorption) were obtained using the Varian Cary5000 UV-Vis-NIR Spectrophotometer (from 300 nm to 800 nm).

X-Ray photoelectron spectroscopy (XPS)

XPS spectra were obtained using a Thermo Fisher Scientific Instrument K-alpha + spectrometer, which consists of a monochromatic Al K-α X-ray source. The XPS data was analysed using Avantage software.

Atomic force microscopy (AFM)

AFM images were obtained using Bruker Dimension Edge (tapping mode). The scanning area for each sample is 30 μm × 30 μm, and the data analysis was made using the Gwyddion software.

Contact Angle

Contact angle measurements were obtained using the Drop Shape Analyser – DSA25, KRISS GmbH. The measurements were taken in the lab air atmosphere using distilled water.

Profilometry

The thickness measurements have been conducted using the Dektak XT (Bruker). The operating mode is Hills and Valleys.

Transmission Electron Microscopy (TEM)

TEM, High-Angle Annular Dark-Field, and Dark-Field Scanning Transmission Electron Microscopy (HAADF-STEM and DF-STEM, respectively) images were obtained using a Thermo-FEI Talos F200i.

View Article Online
DOI: 10.1039/D5TB02697K

Raman Spectroscopy

Raman Spectroscopy measurements were obtained using Horiba Xplora Plus. Raman laser 532 nm and filter 25%.

Distribution of relaxation times (DRT) analysis

DRT analysis was performed in MATLAB R2023b using the DRTTools script[71]. The regularisation parameter was set to 0.01, and the radial basis function was computed using the Full-Width-at-Half-Maximum (FWHM) with a control parameter of 0.3.

Results and discussion

TiO_x films: Materials Characterisation

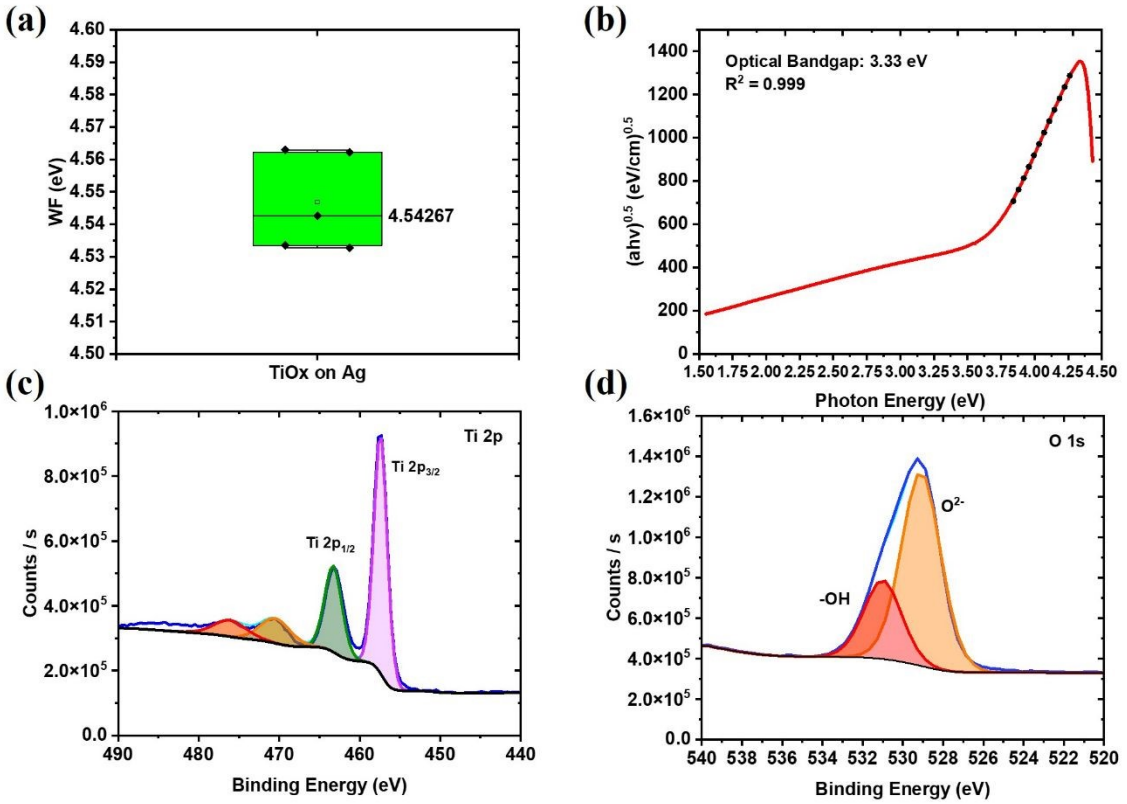

Figure 2. Characterisation methods for the TiO_x films. (a) Kelvin Probe (5 measurements), (b) Tauc Plot, (c) XPS in the area of Ti-related peaks and (d) XPS around the O_2-related peaks. All characterisations lead to the conclusion that TiO_x films are amorphous.

A Kelvin Probe set-up was used to measure the work function WF of TiO_x films deposited on the Ag electrodes because the WF is related to its stoichiometry and the surface potential[72]. The results are shown in Figure 2a. The work function's mean value is 4.54±0.01 eV, which is close to the work function values associated with the TiO_2 anatase phase reported in the literature[72, 73]. However, the e-beam evaporation is a relatively low-energy deposition method,

View Article Online
DOI: 10.1039/D5TB02697K

and combined with the fact that there is no substrate heating[74-76], this result indicates that the TiO_x films are amorphous, which is beneficial for sensing because it suggests a larger specific surface area[77].

UV-Vis absorption measurements were used to determine the optical bandgap of the TiO_x films, whilst the Tauc plot was used to extract the indirect allowed bandgap for the TiO_x films. The results are presented in Figure 2b. The measured optical bandgap of 3.33 eV is slightly higher than the anatase's theoretical value (3.2 eV)[78]; however, it matches the TiO_x bandgap values documented in the literature[79, 80]. This deviation might be related to the amorphous nature or surface oxidation of the TiO_x films. To further prove that the TiO_x films are amorphous, TEM and Raman spectra are presented (see Figure S1). It can be observed that the TiOx films do not have any obvious crystalline morphology, hence the characteristic Raman peaks either do not exist, or they are very broad with very small intensity[81, 82].

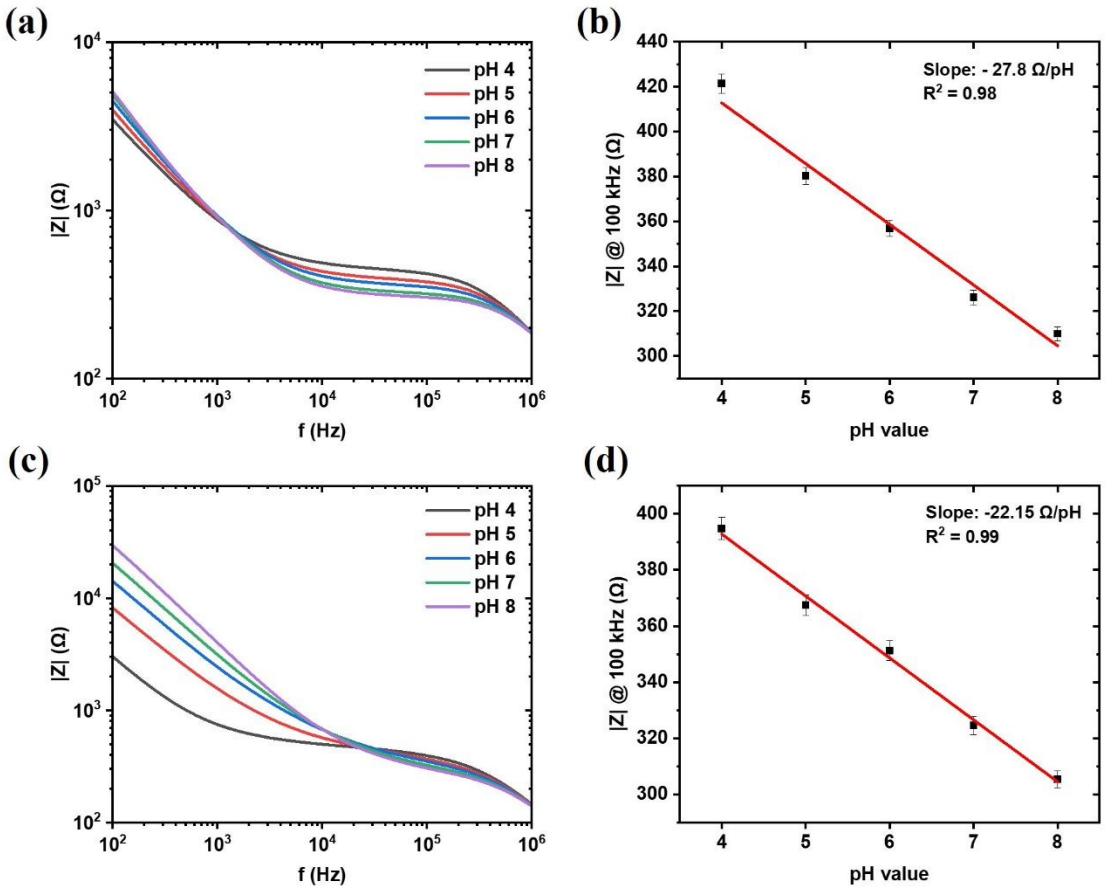

Figure 3. EIS measurements for both TiO_x and PANI sensors in the pH range 4-8. (a) Bode plots for TiO_x sensor, (b) TiOx sensor's impedance linear decrease (-27.8 Ω/pH) at 100 kHz, (c) Bode plots for the PANI sensors and (d) PANI sensor's impedance linear decrease (-22.15 Ω/pH) at 100 kHz. For subfigures (c) and (d), the black dots represent to the average values from n=7 devices.

View Article Online
DOI: 10.1039/D5TB02697K

XPS measurements were performed to investigate the chemical structure of the TiO_x films. The results for the Ti2p area and O1s are presented in Figures 2c and 2d, respectively. It can be observed that two peaks at 458.6 (Full-width-at-half-maximum FWHM 1.3 eV) and 464.2 eV are dominant, which are related to $2p_{3/2}$ and $2p_{1/2}$ orbitals, respectively[83]. Their binding energies and their difference (5.6 eV) – spin-orbit splitting between the doublet peaks – are characteristic of the Ti^{4+} oxidation state[84]. The peaks around 470.8 and 476.5 eV are Ti2p satellite peaks from the TiO_x films. In Figure 2d, there are two peaks, one at 529.2 eV, which is related to the Ti-O bond (lattice oxygen) and another one at 531 eV, related to the -OH groups that are usually present in the TiO_x surface[85].

Sensor response: linearity, sensing mechanism insights and sensing layer thickness independence

The EIS results for the TiOx and PANI sensors (Figure 1) in the pH range 4-8 are shown in Figures 3a-d. The amplitude Bode plots (impedance vs frequency) are presented to study the impedance response of each pH buffer solution on the sensors. The frequency of 100 kHz was selected to study impedance amplitude variations because it is relatively far from the effects of ionic phenomena[49], and it also falls within the plateau region[49] for every pH in the range of 4-8. The TiO_x pH sensors show a sensitivity of -27.8 Ω/pH, while the PANI sensors report a sensitivity of -22.15 Ω/pH, respectively (see Figures 2b and 2d). This sensitivity difference can be correlated with the PANI's doping level, which is kept at 2% wt. The doping selection has been made during the annealing (see Methods) and the electrochemical characterisation steps. The reason is the minimisation of any HCl-related reaction issues on the Ag surface (conversion to AgCl)[86] . The 100 kHz frequency lies within the Bode plateau range, which corresponds to a resistive-double-layer phenomenon, as indicated by the semicircular region in the Nyquist plot (see Figure S2). This implies that any ionic motion processes – reflected by the slope at low frequencies in Figure 2b and the linear part of the Nyquist plot in Figure S2 – have been saturated[87]. Thus, the measured pH sensitivity at 100 kHz can be attributed directly to interfacial phenomena in TiO_x films.

The TiO_x pH interfacial sensing mechanism is based on the semiconductor-electrolyte interface model[88, 89]. In this model, the Fermi level of the sensing layer aligns with the electrochemical potential of the buffer solution, which creates a built-in (flat band) potential. However, because McIlvaine buffer is a non-redox electrolyte, the flat band potential is created by the protonation/deprotonation of the hydroxyl groups (-OH) onto the TiO_x surface (rather

than from the redox species in the traditional models[90]). According to the literature[91], the TiO_x has two acid dissociation constants at pH ~2-5 and 8-9, respectively (which determine the charge net dipole moment and the net surface charge on the TiO_x surface), while the isoelectric point is around pH values 5.6-6.0. The pH range 5-8 lies between the two dissociation constants, hence there is linearity in the frequency range around 100 kHz. On the other hand, the small deviation of the pH 4 case from the linearity can be explained by the fact that this value is closer to a dissociation constant[91] (see Figure 3a). Finally, we conclude that the sensing mechanism of the TiOx film is based on double-layer changes due to protonation/deprotonation, which alter the surface potential of the TiOx film. Following, it can be concluded that studying the pH sensor in the semicircle frequency range, under this sensing mechanism, complies with the Nernst[16] and Bergveld's[44] surface sensing model. This means that measuring the TiO_x impedance sensitivity at 100 kHz is related directly to the surface potential changes (mV/pH) for different pH values.

Therefore, the -OH groups existence onto the TiO_x surface needs to be proven for efficient pH sensing, according to the model described above. The contact angle of water onto the TiO_x surface is found to be 60.2 degrees (see Figure S3), which agrees with the literature[92-94]. This contact angle value proves surface hydrophilicity[95] and is related to the -OH groups on the TiO_x surface[93]. The contact angle (Figure 2), along with the 531 eV peak from XPS measurements (Figure 2d), proves the existence of- OH groups on the TiO_x surface.

The PANI sensing mechanism, on the other hand, is based on the protonation of its polymeric chain[96], it also leads to limited chemical stability as cycling and environmental exposure lead to dopant leaching, oxidation, structural degradation, etc. As pH increases from 4 to 8, hydrogen doping of the conductive PANI-ES chains decreases, until PANI-ES transforms into non-conductive PANI-EB[97]. In this work, HCl doping was used to keep the PANI chains doped; hence, as the H^+ concentration decreases, when pH increases, the detection could still be feasible due to the doping-induced conductivity.

The next step is to establish the surface reversibility during pH measurements. The reversibility in the surface of the TiO_x films implies that there are no surface chemistry changes in the McIlvaine buffer – TiO_x interface. EIS measurements have been obtained in the pH range 4-8, but after every pH value testing, the pH EIS response has been captured at pH 7 (neutral pH value). The results are presented in Figure S4. The linearity remained the same at -27.6 Ω/pH, and the responses at 100 kHz for pH 7 after each buffer solution remained stable. These

View Article Online
DOI: 10.1039/D5TB02697K

results indicate that the TiO_x films undergo reversible surface hydrolysis, according to the protonation-sensing model described above.

EIS was also performed by swapping the Gamry WE and CE probes in the sensor platform to study the sensor's robustness and any Ag parasitic contribution. The results are presented in Figure S5. The Bode plots and the sensitivity remain close to the results from Figure 3a (median sensitivity is -27.33 Ω/pH). This result indicates that, despite the Ag utilisation as a CE, the pH sensing is attributed to the TiO_x film, and any Ag parasitic contribution is either minimal or negligible. This occurs because the TiOx has greater impedance than Ag, hence the TiOx is the dominant sensing-determining layer and is supported by the swapping electrodes experiment. Kramers-Kroning[97] analysis has been executed for pH 4 – 8 EIS spectra. The results can be found in Figure 4a. It can be seen that the data are four to five orders of magnitude less than the impedance values and are randomly distributed around zero, showing no upward or downward trend – strong evidence that the TiO_x sensor is linear and stable.

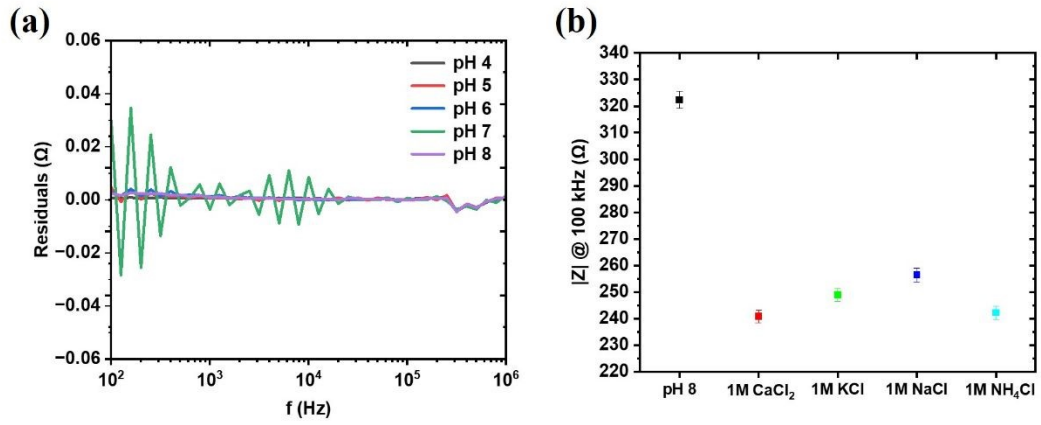

Figure 4. (a) Kramers-Kroning analysis for the TiOx sensor for pH 4-8. No clear tendency signifies the success of this test. (b) The selectivity (20-25% difference from the pH 8 impedance) of the TiOx sensor against chemicals can be found in a wound site. For the subfigure (b), the colour dots correspond to the average values of n=7 devices.

The selectivity of the TiO_x sensor has also been examined against different chemical compounds that can be found in a wound site (i.e. $CaCl_2$[98], KCl[99], NaCl[100], NH_4Cl[101]) with results presented in Figure 4b. At 100 kHz, their impedance response is markedly lower than that of the pH 8 McIlvaine buffer. This is because the different compounds are simple salt solutions, whereas the McIlvaine buffer contains multivalent ions. The resulting increase in the ionic strength reduces the plateau impedance, consistent with the accelerated phenomena on the TiO_x interface[91]. Their impedance is 20% (for the NaCl solution) to 25% (for the $CaCl_2$ solution) lower than that of the pH 8 buffer solution. In other words, the TiO_x pH sensor impedance response to the pH range 4-8 is highly separable from the impedance response of the other salt solutions. These results indicate a selectivity property of the TiO_x films for pH

biosensing. Given that ammonium-related substances are related to bacterial inflammation on the wound site (pH gets alkaline)[101], the NH_4Cl solution's impedance difference from the pH 8 buffer solution gives a potential for an accurate detection of bacterial infection at the wound site.

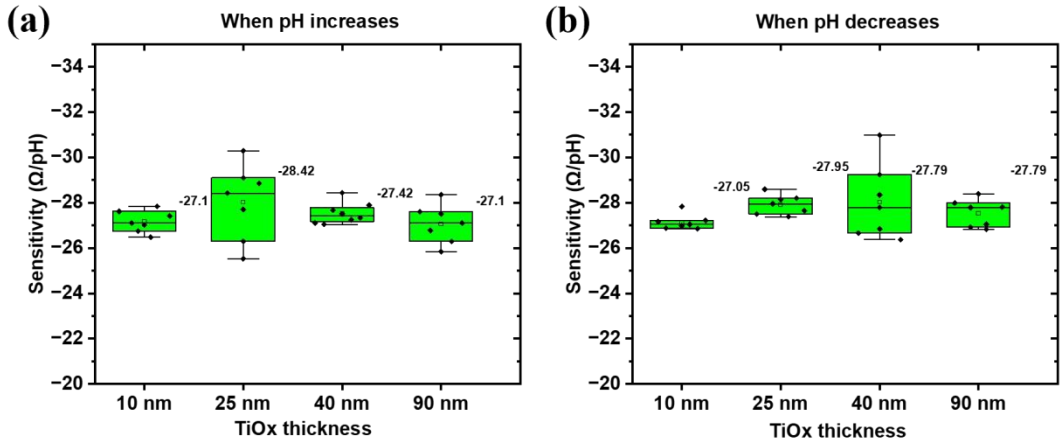

Figure 5. The sensitivity of the pH sensors across different TiO_x thicknesses when (a) pH tested from 4 to 8 and (b) pH tested from 8 to 4, in the same device. The sensitivity remained constant across different TiO_x films' thicknesses. For both the subfigures, the boxplots correspond to the measurements of n=7 devices.

Furthermore, EIS was performed for four different TiO_x thicknesses (10, 25, 40 and 90 nm- please see Figure S6) to prove experimentally that the frequency range chosen for sensitivity measurements is related to interfacial phenomena only. The results in Figure 5a,b show that for either the pH upward (from 4 to 8) or downward testing (from 8 to 4), for all the TiO_x film thicknesses, the pH sensitivity is stable, proving the interfacial nature of the TiO_x films' pH sensing, in the plateau range's 100 kHz frequency. These results indicate that the surface hydrolysis is reversible and thus, the sensitivity is minimally affected by the TiO_x thickness. Additionally, while the EIS ionic component exhibited linear behaviour, its sensitivity (slope) depended on the TiO_x thickness (see Figure S7). This observation can be attributed to the fact that, in these low frequencies, the double layer and the surface reactions described above do not produce any impedance signal. This is because electron kinetics and double layer are fast processes, taking μs to ms, hence their effect on the impedance signal is visible in higher frequencies. Hence, any contribution from the film resistance becomes the dominant factor since the proton-transfer effects are present in the transport-limiting regime. Consequently, the rate-determining factor shifts from the interfacial double-layer to the ionic diffusion to the electrode and film resistance, leading to a variable sensitivity in this frequency range.

pH detection at a 0.5-fold diluted McIlvaine buffer solution

View Article Online
DOI: 10.1039/D5TB02697K

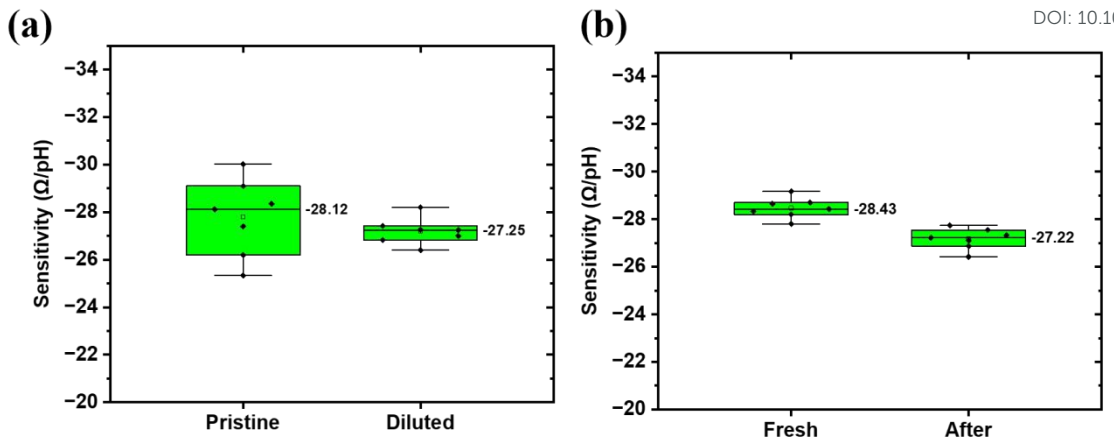

Figure 6. (a) The sensitivity of the TiO_x sensors for the pristine vs 0.5-fold diluted McIlvaine buffer solution. The TiO_x sensors maintained 96.9% of their sensitivity vs the pristine buffer solutions. (b) The sensitivity of the TiO_x fresh vs thermal annealed pH sensors. A 95.7% sensitivity recovered after the thermal annealing treatment. For both the subfigures, the boxplots correspond to the measurements of n=7 devices.

The EIS response of the TiO_x sensors has been examined under 0.5-fold diluted McIlvaine buffer solutions. The reason behind this experiment is to test the TiO_x sensor's pH sensitivity limits (proton detection). The results are presented in Figure 6a. It can be observed that the sensitivity retained 96.9% of its value relative to the pristine buffer solution (see Figure 3a). This indicates that the sensor maintained its interfacial pH sensitivity with lower H^+ concentration. Hence, the TiO_x sensor has the capability of accurate pH detection in lower concentration aquatic media. The sensitivity's consistency under 0.5-fold dilution demonstrates that the TiO_x sensors have a potential for operating in environments with minimum proton concentrations.

Recyclability – Recovery after thermal annealing

The sensor's response was examined after a period of approximately 3 months (stored in cleanroom conditions) after fabrication to investigate its long-term functionality (see Figure 6b). Given the chemical degradation and the one-month timeframe used to classify a wound as chronic, it is pertinent to investigate whether the TiO_x sensor can recover its sensitivity after long periods (2-3 months). After three months of fabrication, there was no linearity in the pH range 4-8. After thermal annealing at 200℃ for 2 hours, the sensor sensitivity has been retained at 95.7% (-27.1 Ω/pH median value) of the sensitivity of the fresh TiO_x devices (-28.3 Ω/pH median value). Before and after annealing, AFM was used to investigate any morphological surface modifications to the Ag thin film electrodes, with the results shown in Figure S8. The surface roughness increased from 2 nm to 6.4 nm RMS without any indication of island formation. At 200℃, the Ag tends to form larger grains, resulting in increased surface

roughness[102]. This demonstrates that the TiO_x sensor can have an extended lifetime, which reduces the waste and maintenance costs.

Time stability

The performance of the TiOx and PANI pH sensors was tested for 31 days (approximately the time required to determine whether a wound is chronic). In the first test type of stability (see Methods - impedance value vs time for pH 4 and 8, respectively), the impedance at 100 kHz was tested using only pH 4 and pH 8 buffer solutions every time, for both TiO_x and PANI sensors. Regarding the pH 4-related time stability (see Figure 7a), after 31 days, TiO_x sensors showed an impedance increase of 5.65% (from 424.2 Ω to 448.2 Ω median values) while the PANI impedance increased 10.55% (from 393.2 Ω to 434.7 Ω median values). PANI chain is more prone to oxidation than TiO_x, which is already in an oxidised state, as a metal oxide, which leads to chemical degradation, after consistent exposure to pH 4.

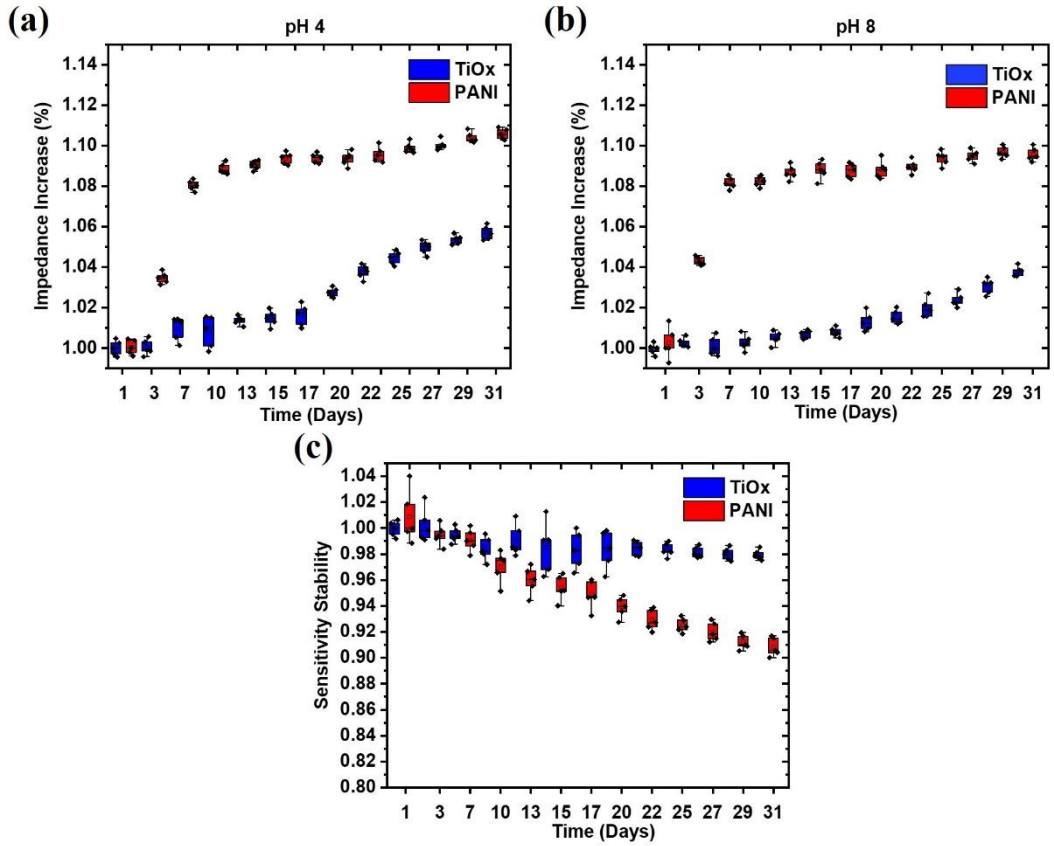

Figure 7. The one-month time stability results for both the TiO_x and PANI sensors. (a) Measuring Impedance at 100 kHz with pH 4 buffer solution only. TiO_x sensors report 5.65% increase while the PANI 10.55%. (b) Measuring Impedance at 100 kHz with pH 8 buffer solution only. TiO_x sensors report 3.8% increase while the PANI 9.46%. (c) Measuring the sensitivity over time. The TiOx sensors lost only 2.25% of their sensitivity while the PANI lost 10% of its sensitivity. These percentages are calculated using the median values from the boxplots. For all the subfigures, the boxplots correspond to the measurements of n=5 devices.

For pH 8, the time stability results showed that the impedance of the TiO_x sensors increased (see Figure 7b) by 3.8% (from 316.3 Ω to 328.4 Ω median values) while the impedance of the

View Article Online
DOI: 10.1039/D5TB02697K

PANI sensors increased by 9.46% (from 305.4 Ω to 334.3 Ω median values). The time stability at pH 8 of TiO_x sensors is expected to be higher than that of PANI at pH 8, since PANI undergoes a transition from the ES to EB form. At this stage, its conductivity can only be maintained through HCl doping[103]. The consistent exposure of PANI at pH 8 probably leads to a partial degree of dedoping near the surface. Generally, lower degradation in the pH 8 experiments relative to the pH 4 experiments is expected because higher acidity leads to a higher concentration of H+, which promotes irreversible hydrolysis, backbone degradation (especially for PANI), and dissolution of atoms (especially for amorphous TiO_x).The results for the second test of stability (see Methods - impedance slope at 100 kHz vs time) are

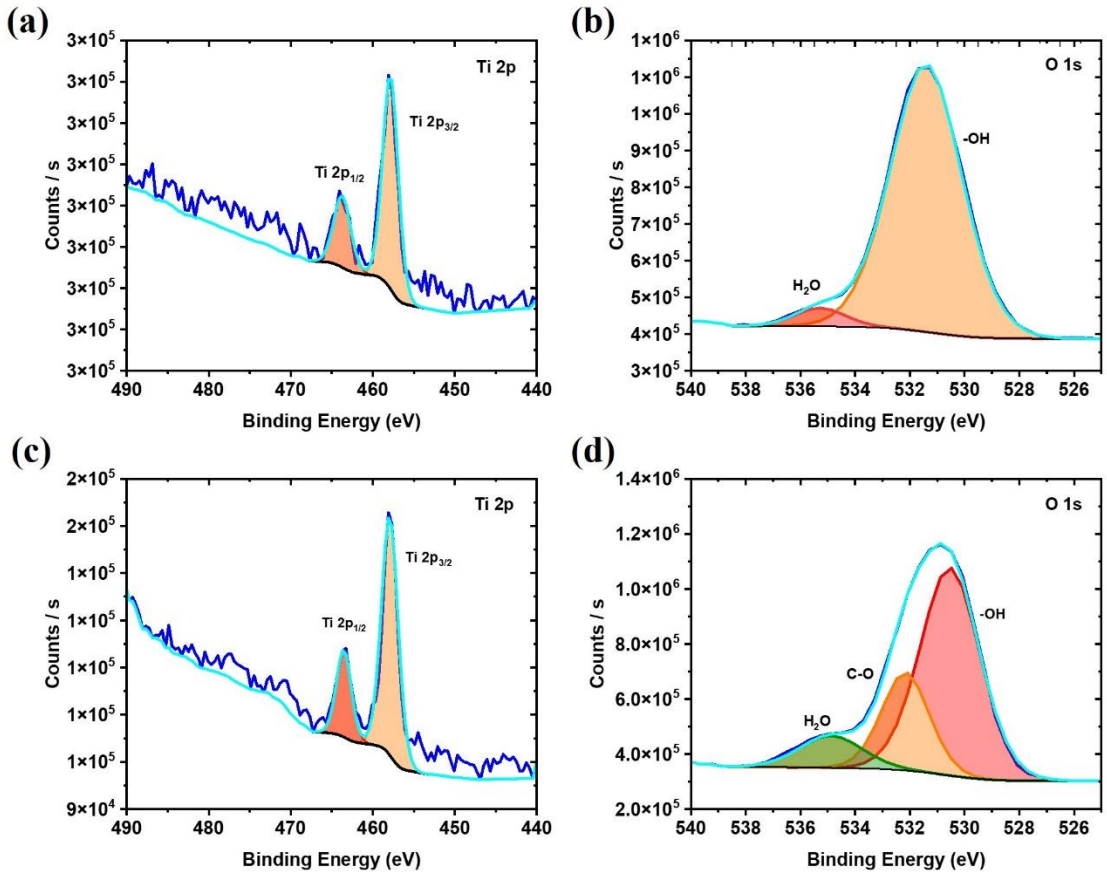

Figure 8. XPS measurements, for the TiO_x sensors, after the one-month stability at measuring impedance only with (a-b) pH4 and (c-d) pH 8 buffer solution, respectively. The Ti $2p_{3/2}$ (~458.8 eV) peak position remain constant while the -OH related peak (~531 eV) increased vs the one in Figure 2. This means that the stichoimetry of the film mentained but water chemisorbed on the surface after the stability experiments.

presented in Figure 7c. After 31 days, the TiO_x pH sensors lost only 2.25% of their sensitivity (from -27.45 Ω/pH to -26.86 Ω/pH median values) while the PANI pH sensors lost ~10% of their sensitivity (from -22.21 Ω/pH to -20.05 Ω/pH median values). The reason behind this difference, except for the HCl partial dedoping, is that PANI is also more prone to degradation in air and humidity than TiO_x, as an organic polymer[103]. Finally, statistical tests, at 95 %

View Article Online
DOI: 10.1039/D5TB02697K

significance level, were performed on the datasets above (please see Statistical Analysis Section in the Supplementary Information). The null hypothesis testing (2-sample t-test) will provide information for the statistical significance between the mean values of every dataset, or if any variations arise from random noise. Rejection of the null hypothesis ($h = 1$, $p < 0.05$) will be used to confirm statistically significant differences in the EIS pH sensor responses. The EIS data from Figures 3b and 3d are statistically significant, hence the EIS data are realistic, highlighting the interfacial capacitive-resistive phenomena on the sensors' surfaces. The data from Figures 5a, 5b and 6a show little statistical significance, which is beneficial for our sensor because they cross-validate that the sensitivity of the TiO_x film is thickness-independent. The dilution of the buffer solution causes a minimum effect on the TiO_x sensor performance, as well. The data from recovery after annealing and 31-day stability (Figures 6b, 7a,b,c) show statistical significance at 95% level. This means that these EIS data are reliable (not statistical noise) and cross-validate the greater TiO_x pH sensor time stability performance versus the PANI pH sensors.

We used XPS to investigate potential chemical structural changes at the TiOx film surface after 31 days of stability (continuous exposure to pH 4 and pH 8 buffer solutions). The results for the Ti2p and O1s areas are presented in Figure 8. In Figures 8a,c, the Ti2p peak positions are for pH 4, at 458.8 eV (FWHM 1.3 eV) and 464.5 eV and for pH 8, at 458.7 eV (FWHM 1.3 eV) and 464 eV. The $Ti2p_{3/2}$ peak position and FWHM remain relatively stable, close to those reported for the fresh device (Figure 2c), indicating that any change in the Ti oxidation state (such as oxygen deficiency) is negligible. In Figures 8b,d, a shift in the O1s peak can be detected from 529.2 eV to 531.3 eV. This can be attributed to the fact that after one-month experiments, there is water adsorbed onto the TiO_x surface (hydroxylated surface) because McIlvaine buffer is a water-based buffer solution, but the stoichiometry is maintained. The observed oxygen peak shift can explain the recyclability in Figure 6b. The identified hydroxylated species and residual buffer compounds adsorbed on the TiO_x surface, following the pH measurements and ageing. The efficacy of the thermal annealing treatment for the regeneration is well-documented, as it removes such humidity-related contaminants from metal oxide surfaces[104-106].

The series resistance after 31 days has been studied as well (the real axis' shift at the Nyquist plot) to investigate any degradation of the Ag CE, which can distort the impedance signal. For

View Article Online
DOI: 10.1039/D5TB02697K

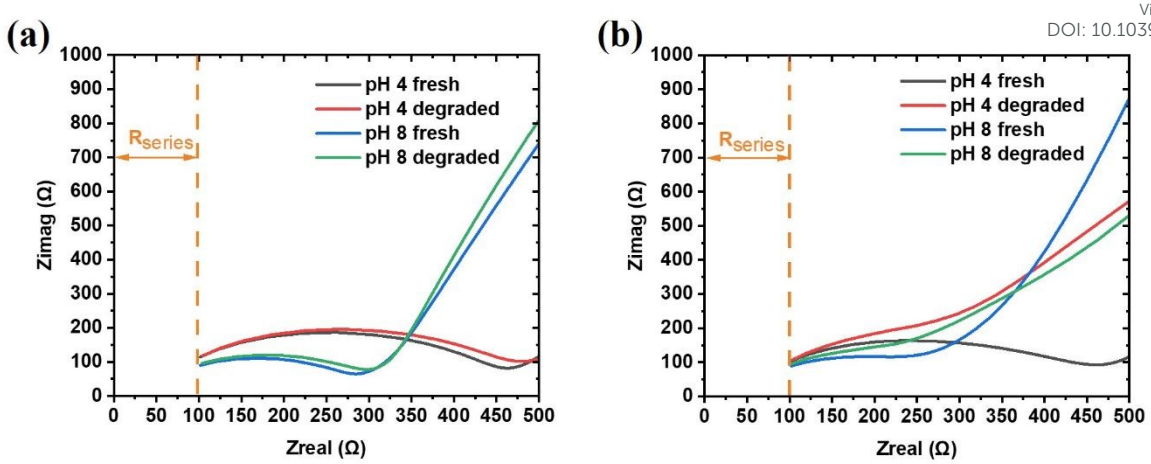

Figure 9. Electrode's degradation for pH 4 and pH 8- stability experiments, for (a) the TiO_x sensors and (b) the PANI sensors. An Ag electrode degradation less than 2.3% is reported for all cases.

the 2-electrode TiO_x sensor, the Nyquist plot's real axis shift can be correlated with the electrodes' (series) resistance and thus, its degradation[107] when it is increased. In EIS measurements, the series resistance can be found from the curve shift on the real axis. The results for the first type of time stability, for both TiO_x and PANI pH sensors, are presented in Figures 9 and S9. For the TiO_x sensor, the series resistance increase is 2.3% (from 101.84 Ω to 104.2 Ω) for the pH 4 case, and 1.7% (from 109.54 Ω to 111.44 Ω) for the pH 8 case, respectively. For the PANI sensor, the series resistance increase is 1.94% (from 101.6 Ω to 103.58 Ω) for the pH 4 case, and 1.5% (from 108.96 Ω to 110.66 Ω) for the pH 8 case, respectively. In Figure S9, the Nyquist plots for the pH 4 and pH 8 diluted buffer solutions are presented. The shift on the real axis is 100 Ω and 109 Ω for the pH 4 and pH 8, respectively. These results indicate that the Ag electrode undergoes minimal corrosion during EIS measurements. Thus, the sensor's capability for long-term stability assessment, using Ag as an electrode material, has been demonstrated. This can be attributed to the low-voltage, low-current nature of EIS, which generates only a weak electric field in the electrochemical cell. As a result, the ions lack sufficient energy to undergo parasitic reactions with either the sensing films or the metal electrodes. Finally, the above results (Figure 9), along with the electrode swapping and the Kramers-Kroning analysis (Figure 4), indicate that Ag can be used as an electrode material for pH sensing, further highlighting the TiO_x sensor as a low-cost, sustainable pH sensor.

DRT Analysis

The DRT analysis is an established model-free method used frequently to study electrochemical systems and analyse EIS data without any use of equivalent circuits and a priori knowledge of the processes that take place. Especially in this paper, where a 2-electrode

View Article Online
DOI: 10.1039/D5TB02697K

system is used, the equivalent circuit more complex than the Randles circuit. In this paper, DRT is utilised to validate that the pH sensor's response is based on the interface phenomena.

The results for both TiO_x and PANI are presented in Figure S10. Both figures exhibit two characteristic peaks in the distribution: one around 10^{-6} sec (fast process) and one at 5×10^{-3} sec (slow process). These peaks are related to resistive-capacitive phenomena and diffusion processes, respectively[56]. Briefly, these figures show the contribution of each electrochemical

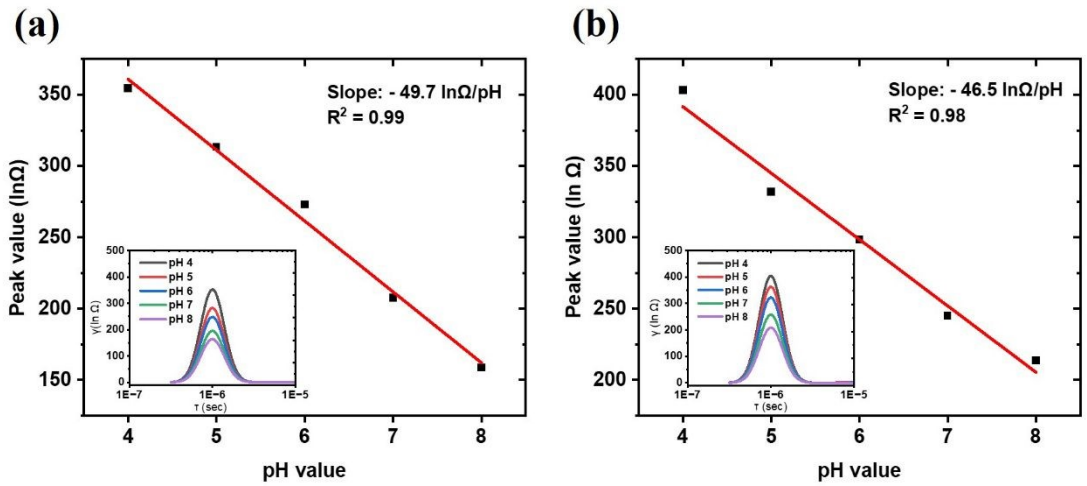

Figure 10. DRT data in the region related to the resistive-capacitive phenomena for (a) the TiO_x and (b) PANI pH sensors. The peak values show a linear decreasing trend, as pH increases, which validates the interfacial behaviour of the pH sensing. Insets: The DRT curves for each pH sensor in the area related to the resistive-capacitive phenomena.

process's impedance to the total cell impedance. The intensity of the fast process (<500 lnΩ) is always lower than that of the slow process (>1500 lnΩ). This observation can be correlated with Bode plots' frequency range 100 Hz – 1MHz (see Figure 2) and the curve's downward bending (due to the pole) after 100 kHz. Thus, this downward bending in the Bode plots exists in a small frequency range (> 100 kHz to 1 MHz) relative to the whole frequency range (100 Hz to 1 MHz). The impedance in this area is almost one order of magnitude lower than the impedance in the diffusion section of the spectra (< ~10 kHz). Moreover, the diffusion-related area has two overlapping peaks, probably because the extrapolation or overlapped ionic processes cannot be detected in the Nyquist plot (because the slope at the Nyquist plot remains constant, see Figure S2).

In Figures 10a and 10b, the peak values in the area related to the resistive-capacitive phenomena are shown. Both TiO_x and PANI show a linear decrease (-49.7 lnΩ/pH and – 46.5 lnΩ/pH for the TiO_x and PANI pH sensors, respectively) in peak height. This linearity is a strong indicator that the pH sensing, both for the TiO_x and PANI, is an interfacial phenomenon related to resistive-capacitive phenomena. This observation agrees with the literature on pH

View Article Online
DOI: 10.1039/D3TB02697K

models for Transition Metal Oxides and surface potential, as described in a previous section. Overall, with no a priori assumptions, DRT analysis shows a linear response in the relaxation time area related to interfacial phenomena, validating the analysis in the section above and the selection of 100 kHz for studying the sensor sensitivity. An equivalent circuit (transfer function) analysis has been executed to interpret the DRT analysis data (please see Figure S11, Equivalent Circuit Analysis section – Supplementary Information). Two district time-constant values have been derived and can be related to diffusion and interfacial phenomena in the pH range 4-8. DRT and equivalent circuit analysis are partially complementary; however, DRT's continuous γ function provides a more detailed presentation of (overlapping) relaxation processes and their characteristic time constants (Figure 10 and S10).

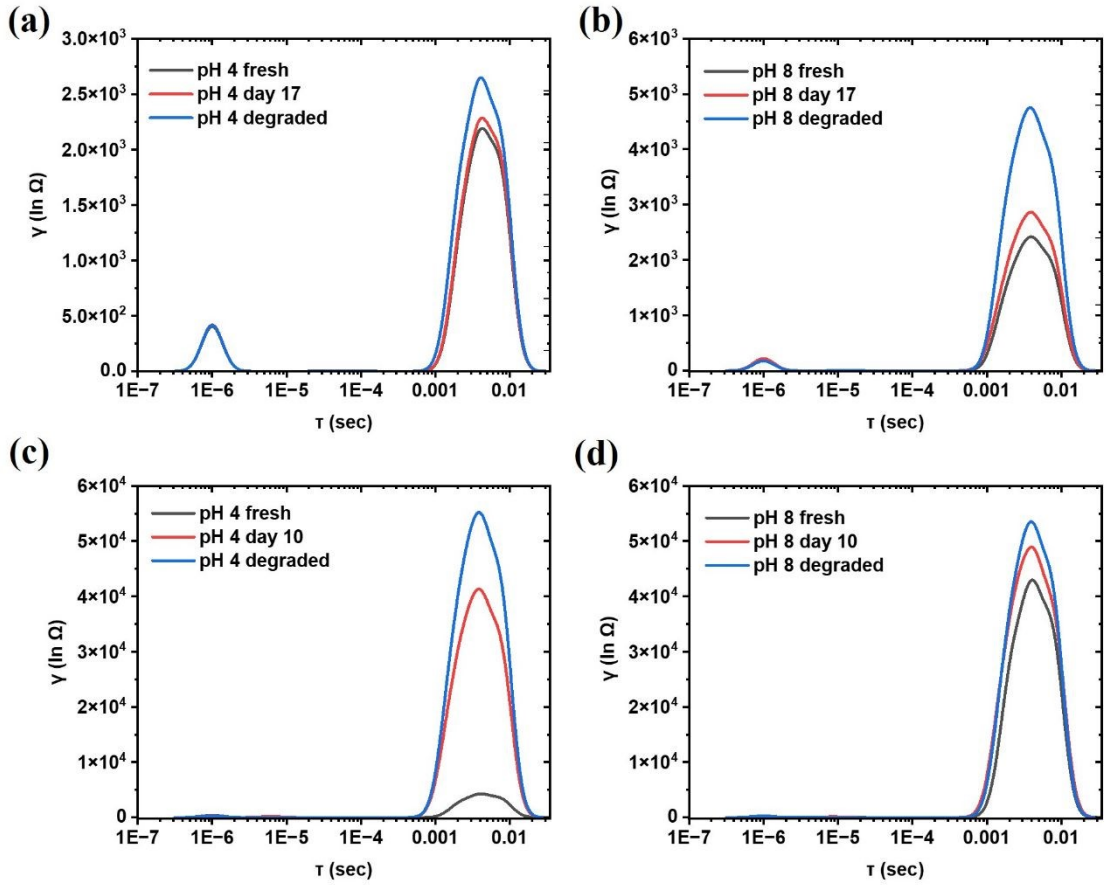

Figure 11. DRT analysis for the pH 4 and pH 8- degradation studies. An increase over time, in the area of the ionic-related motion phenomena, is presented because of the surface contamination.

Furthermore, DRT analysis was used on the EIS results from the first type of stability experiments to identify any changes in the distribution of relaxation times. The results are shown in Figures 11a,b and 11c,d for TiO_x and PANI, respectively (please find the equivalent circuit analysis and the time-constant calculation in the relevant section of the Supplementary Information). For both TiO_x and PANI, it can be observed that the diffusion-related area is

View Article Online
DOI: 10.1039/D5TB02697K

increasing (its relaxation time becomes more dominant) after degradation. This can be explained by the fact that the interface is degraded (water chemisorption, see Figure 8), hence the interaction (sensing mechanism) between the buffer solution and the -OH groups of the TiO_x films is diminished. To cross-validate these findings, the Bode plots for both pH 4 and 8 are presented in Figure S10. The correlation between these results (Figures 11 and S12) has also been seen in another TMO-based work[41]. For TiO_x, for both pH 4 and 8, the low-frequency line gradually shifts progressively toward higher frequencies. This translates to the fact that diffusion becomes the dominant process in this frequency spectrum[107]. This, in turn, has a substantial impact on the interfacial phenomena such as the double layer and charge transfer (which, in our study, affect the sensitivity of the pH sensor). For PANI, for both pH 4 and 8, there is again a low-frequency line shift towards the high frequencies. It can be noticed that for pH 4, this shift is almost one order of magnitude, marking the reason for such a high peak increase in Figure 11c and its impact on the PANI surface and its corresponding drop in sensitivity (Figure 7c).

Moreover, the effect of the adsorbed water (to explain the observations from Figure 11) on the impedance of the TiO_x film, at 100 kHz, has been examined. For this purpose, the HAADF-STEM and DF-STEM of the TiO_x film's surface are provided in Figure S13. These images show non-uniform densities of the order of nanometres (where HAADF contrast is proportional to density thickness and Z^2, and Z is taken constant). Adsorbed water can affect the porosity of the TiOx film and potentially influence the interfacial sensing phenomenon. Here, as porosity, we define the defect states in the amorphous TiO_x film, ranging from oxygen vacancies as trap states - their potential contribution to the interfacial capacitive-resistive phenomena - (see Figures 3, 10, 11 and S10) to nano-metre scale non-uniformities (STEM images, Figure S13), and to adsorbed water species (see XPS data, Figure 8b,d). Hence, the approach of the constant-phase element (CPE)-like phase parameter α is used[108, 109]. The results are presented in Figure S14. The position and the magnitude of α remain nearly unchanged across the sensor states (fresh, degraded, and annealed). The EIS 100 kHz working frequency lies close to the minimum for both pH 4 and 8, where the slope is minimal. This means that the TiO_x pH sensor response at 100 kHz is relatively insensitive to interfacial variations, including effects on film porosity. Consequently, even though adsorbed species affect diffusion-related processes (Figure 11), their effect on the sensitivity remains limited. This interpretation is consistent with our experimental observations, including the DRT analysis (Figure 11a, b), and the sensitivity retention and recovery values (97.75% and 95.7%, respectively; Figures 7c and 6b).

View Article Online
DOI: 10.1039/D5TB02697K

Finally, after presenting the stability results (Figure 7) and validating them with DRT analysis (Figure 11), it can be concluded that the proposed low-cost TiOx pH sensor has a competitive operational lifetime compared with the high-cost pH sensors reported in the literature (please see Table S1). Also, the stability protocol presented in this paper examines both sensitivity and edge values over time. This gives a broader knowledge of the pH sensor lifetime, and thus, its translation potential to a smart bandage.

Conclusion

In this paper, an impedimetric TiO_x pH sensor has been presented. The sensor exhibited linearity of –27.8 Ω/pH across the clinically relevant pH range of 4–8, which is critical for chronic wound monitoring. The TiO_x pH sensor's time (chemical) stability has been examined versus PANI. After one month of operation—the period for defining wound chronicity—the TiO_x sensor lost only 2.25% of its initial sensitivity. In contrast, the state-of-the-art material PANI showed a 10% loss in sensitivity under the same conditions. In pH 4 and 8 studies, the PANI sensor showed an impedance increase (10% and 9% increase for pH 4 and 8, respectively), almost double that of the TiO_x sensor (5.5% and 4% increase for pH 4 and 8, respectively). The stability studies highlight TiO_x's chemical interfacial stability after continuous exposure to acidic and alkaline media, compared with PANI. Analysis from both Bode and Nyquist plots revealed the interfacial nature of the pH sensing, as well as its reversibility and recyclability. The TiO_x pH sensor recovered 95.7% of its sensitivity after 200℃ thermal annealing, further demonstrating its robustness. These results underscore the greater demonstrated chemical stability of the lower-cost TiO_x compared to PANI. Minimal Ag corrosion and interference were observed in the pH sensing, further indicating the TiO_x pH sensor's suitability in low-cost and sustainable sensing applications, whereas state-of-the-art PANI-based pH sensors cannot be utilised because of their cost. Finally, DRT analysis has been utilised as a model-free approach to cross-validate the interfacial nature of sensing and the degradation mechanism, both for TiO_x and PANI films. In this work, photolithography and e-beam evaporation were used to fabricate the TiO_x pH sensor prototype. Fabrication can also be achieved using solution-processed methods (such as spray coating for the TiOx) and printed electronics methods (such as inkjet or screen printing for the Ag electrodes). The future direction of this work is to test the prototype TiO_x sensor's performance in complex biological environments with bacterial infection and to integrate it into a smart bandage. Towards clinical translation, the prototype TiOx pH sensor should be tested using cytotoxicity assays, such as the MTT assay, to evaluate the sensor's biocompatibility. This work provides an important

View Article Online
DOI: 10.1039/D5TB02697K

demonstration towards long-term and low-cost pH biosensing. Hence, a pathway to more robust biosensor data is an optimistic indicator for the deployment of smart bandages to real-world applications.

Author Contributions

Conceptualisation: K.A., A.P. and G.K. Discussion, Literature analysis: K.A., A.P., G.K, S.R.P.S. and V.S. K.A. designed, fabricated, characterised the devices, conducted EIS experiments, DRT analysis and analysed the data. A.P, K.A. conducted UV-Vis and Contact Angle measurements. A.P. conducted AFM measurements. L.A. conducted Kelvin Probe measurements. X.P. prepared the schematics. D.I.K. prepared the evaporation masks. S.J.H. conducted XPS measurements and the first peak analysis. K.A. conducted the Raman Spectroscopy Measurements. V.S executed the TEM, HAADF-STEM, and DF-STEM imaging. First Draft writing: K.A. Review and editing: A.P., G.K, S.R.P.S. and V.S. Supervision: V.S. and S.R.P.S. Funding acquisition: V.S. and S.R.P.S. All authors have read and agreed to the submission of the manuscript.

Conflicts of interest

There are no conflicts to declare.

Data availability

The data supporting this article have been included as part of the Supplementary Information.

Acknowledgements

For open access purposes, the authors have applied a Creative Commons attribution license (CC BY) to any Author-Accepted Manuscript version arising from this submission. The authors would like to extend their appreciation to the University of Surrey for the doctoral scholarship of K.A.

References

1. R. G. Frykberg and J. Banks, *Advances in Wound Care*, 2015 Sep 1, **4**.
2. A. K. S. Iversen, M. Lichtenberg, B. G. Fritz, I. D.-P. Cort, D. F. Al-Zoubaidi, H. Gottlieb, K. Kirketerp-Møller, T. Bjarnsholt and T. H. Jakobsen, *BMJ Open*, 2024-10-01, **14**.
3. A. Horta-Velázquez, J. D. Mota-Morales and E. Morales-Narváez, *International Journal of Biological Macromolecules*, 2024/01/01, **254**.
4. D. H, K. SS, A. F, G. IO and T. A, *Trends in biotechnology*, 2018 Dec, **36**.
5. N. Brasier, J. Wang, W. Gao, J. R. Sempionatto, C. Dincer, H. C. Ates, F. Güder, S. Olenik, I. Schauwecker, D. Schaffarczyk, E. Vayena, N. Ritz, M. Weisser, S. Mtenga, R. Ghaffari,

J. A. Rogers, J. Goldhahn, N. Brasier, J. Wang, W. Gao, J. R. Sempionatto, C. Dincer, H. C. Ates, F. Güder, S. Olenik, I. Schauwecker, D. Schaffarczyk, E. Vayena, N. Ritz, M. Weisser, S. Mtenga, R. Ghaffari, J. A. Rogers and J. Goldhahn, *Nature 2024 636:8041*, 2024-12-04, **636**.

6. S. Cheng, Z. Gu, L. Zhou, M. Hao, H. An, K. Song, X. Wu, K. Zhang, Z. Zhao, Y. Dong and Y. Wen, *Frontiers in Bioengineering and Biotechnology*, 2021 Nov 1, **9**.
7. C. Yang, C. Yang, Y. Chen, J. Liu, Z. Liu and H.-J. Chen, *Journal of Science: Advanced Materials and Devices*, 2023/12/01, **8**.
8. W. C, S. S. E, S. CD, L. CT, W. J, A. DG and G. W, *Nature reviews. Materials*, 2024 Aug, **9**.
9. F. Wang, Y. Xie, W. Zhu, T. Wei, F. Wang, Y. Xie, W. Zhu and T. Wei, *Chemosensors 2023, Vol. 11, Page 481*, 2023-09-01, **11**.
10. A. Barhoum, S. Hamimed, H. Slimi, A. Othmani, F. M. Abdel-Haleem and M. Bechelany, *Trends in Environmental Analytical Chemistry*, 2023/06/01, **38**.
11. J. Wu, H. Liu, W. Chen, B. Ma, H. Ju, J. Wu, H. Liu, W. Chen, B. Ma and H. Ju, *Nature Reviews Bioengineering 2023 1:5*, 2023-02-24, **1**.
12. *Journal of Biomedical Materials Research Part B: Applied Biomaterials*, 2014, **102**.
13. C. Tate, R. Wang, S. Akaraci, C. Burns, L. Garcia, M. Clarke and R. Hunter, *Cities*, 2024/02/01, **145**.
14. L. A. Schneider, A. Korber, S. Grabbe, J. Dissemond, L. A. Schneider, A. Korber, S. Grabbe and J. Dissemond, *Archives of Dermatological Research 2006 298:9*, 2006-11-08, **298**.
15. S. S. E, X. C, W. C, S. Y, M. J, T. J, S. SA, L. J, B. JL, A. DG and G. W, *Sci Adv*, 03/24/2023, **9**.
16. H. J. Park, J. H. Yoon, K. G. Lee and B. G. Choi, *Nano Convergence*, 2019 Mar 18, **6**.
17. G. P. Neupane, W. Ma, T. Yildirim, Y. Tang, L. Zhang and Y. Lu, *Nano Materials Science*, 2019/12/01, **1**.
18. Z. Wang, X. Wu, S. Zhang, S. Yang, P. Gao, P. Huang, Y. Xiao, X. Shen, X. Yao, D. Zeng, J. Jie, Y. Zhou, F. Yang, R. Li, W. Hu, Z. Wang, X. Wu, S. Zhang, S. Yang, P. Gao, P. Huang, Y. Xiao, X. Shen, X. Yao, D. Zeng, J. Jie, Y. Zhou, F. Yang, R. Li and W. Hu, *Proceedings of the National Academy of Sciences*, 2025-4-3, **122**.
19. C. G. Tang, K. Hou and W. L. Leong, *Chemistry of Materials*, December 18, 2023, **36**.
20. M. S. Hossain, N. Padmanathan, M. M. R. Badal, K. M. Razeeb and M. Jamal, *ACS Omega*, September 12, 2024, DOI: 10.1021/acsomega.4c06090.
21. J. Min, S. Demchyshyn, J. R. Sempionatto, Y. Song, B. Hailegnaw, C. Xu, Y. Yang, S. Solomon, C. Putz, L. E. Lehner, J. F. Schwarz, C. Schwarzinger, M. C. Scharber, E. Shirzaei Sani, M. Kaltenbrunner, W. Gao, J. Min, S. Demchyshyn, J. R. Sempionatto, Y. Song, B. Hailegnaw, C. Xu, Y. Yang, S. Solomon, C. Putz, L. E. Lehner, J. F. Schwarz, C. Schwarzinger, M. C. Scharber, E. Shirzaei Sani, M. Kaltenbrunner and W. Gao, *Nature Electronics 2023 6:8*, 2023-07-20, **6**.
22. X. Zhu, X. Zhu, H. Sun, H. Sun, B. Yu, B. Yu, L. Xu, L. Xu, H. Xiao, H. Xiao, Z. Fu, Z. Fu, T. Gao, T. Gao, X. Yang and X. Yang, *RSC Advances*, 2024/02/07, **14**.
23. J. Lee, L. M. Liberty, I. Soltis, K. Kwon, D. Chong, Y. Kwon and W.-H. Yeo, *ACS Applied Materials & Interfaces*, May 10, 2025, **17**.
24. Y. Ding, Y. Ding, W. Liu, W. Liu, Z. Xu, Z. Xu, Z. Duan and Z. Duan, *Journal of Materials Chemistry A*, 2024/08/06, **12**.

25. R. V. Mom, L. J. Falling, O. Kasian, G. Algara-Siller, D. Teschner, R. H. Crabtree, A. Knop-Gericke, K. J. J. Mayrhofer, J.-J. Velasco-Vélez and T. E. Jones, *ACS Catalysis*, April 15, 2022, **12**.
26. I. A. Ges, B. L. Ivanov, D. K. Schaffer, E. A. Lima, A. A. Werdich and F. J. Baudenbacher, *Biosensors and Bioelectronics*, 2005/08/15, **21**.
27. J. Chu, Y. Zhao, S.-H. Li, H.-Q. Yu, G. Liu and Y.-C. Tian, *Electrochimica Acta*, 2015/01/10, **152**.
28. O. Concepción, O. d. Melo, O. Concepción and O. d. Melo, *Journal of Physics: Condensed Matter*, 2023-02-16, **35**.
29. *Chemical Reviews*, 2014, **114**.
30. U. Diebold, *Surface Science Reports*, 2003/01/01, **48**.
31. J. Wang, J. Xiong, H. Guo and Y. Wei, *ChemCatChem*, 2024/10/21, **16**.
32. V. S. Saji and C.-W. Lee, *ChemSusChem*, 2012/07/01, **5**.
33. M. Solanki, U. Parihar, K. Patel, V. Jain, S. S. Sharma and J. Ray, *Chemical Physics Impact*, 2025/06/01, **10**.
34. A. A. Shaikh, J. Bhattacharjee, P. Datta and S. Roy, *Sustainable Chemistry for the Environment*, 2024/09/01, **7**.
35. A. Panagiotopoulos, A. Panagiotopoulos, G. Kakavelakis, G. Kakavelakis, K. Almpanidis, K. Almpanidis, L. Askew, L. Askew, D. I. Kutsarov, D. I. Kutsarov, S. R. P. Silva and S. R. P. Silva, *Journal of Materials Chemistry A*, 2025/03/18, **13**.
36. E. S. Yoon, H. J. Park, M. S. Kil, J. Kim, K. G. Lee and B. G. Choi, *Bulletin of the Korean Chemical Society*, 2023/06/01, **44**.
37. J. Lee, I. Soltis, S. A. Tillery, S. H. Lee, H. Kim and W.-H. Yeo, *Biosensors and Bioelectronics*, 2024/06/15, **254**.
38. H. J. Park, J. H. Yoon, K. G. Lee, B. G. Choi, H. J. Park, J. H. Yoon, K. G. Lee and B. G. Choi, *Nano Convergence 2019 6:1*, 2019-03-18, **6**.
39. A. K. Pathak, V. Bhardwaj, R. K. Gangwar, M. De and V. K. Singh, *Optics Communications*, 2017/03/01, **386**.
40. M. J. Schöning, D. Tsarouchas, L. Beckers, J. Schubert, W. Zander, P. Kordoš and H. Lüth, *Sensors and Actuators B: Chemical*, 1996/09/01, **35**.
41. M. Zea, A. Moya, M. Fritsch, E. Ramon, R. Villa and G. Gabriel, *ACS Applied Materials & Interfaces*, March 8, 2019, **11**.
42. J. Wang, C. Wu, N. Hu, J. Zhou, L. Du, P. Wang, J. Wang, C. Wu, N. Hu, J. Zhou, L. Du and P. Wang, *Biosensors 2012, Vol. 2, Pages 127-170*, 2012-04-25, **2**.
43. *Fundamentals of Nanoparticles*, 2018, DOI: 10.1016/B978-0-323-51255-8.00017-3.
44. P. Bergveld, *Sensors and Actuators B: Chemical*, 2003/01/01, **88**.
45. S. Wang, J. Zhang, O. Gharbi, V. Vivier, M. Gao and M. Orazem, *NATURE REVIEWS METHODS PRIMERS*, 2021, **1**.
46. J. Wu, *Chemical Reviews*, May 20, 2022, DOI: 10.1021/acs.chemrev.2c00097.
47. S. Åberg, *Journal of Electroanalytical Chemistry*, 1997/12/10, **439**.
48. H. C. Lim, J.-E. Park, J.-I. Hong and I.-S. Shin, *Bulletin of the Korean Chemical Society*, 2020/03/01, **41**.
49. H. S. Magar, R. Y. A. Hassan, A. Mulchandani, H. S. Magar, R. Y. A. Hassan and A. Mulchandani, *Sensors 2021, Vol. 21, Page 6578*, 2021-10-01, **21**.
50. A. M. Manoj and L. R. Viannie, *Electroanalysis*, 2023/11/01, **35**.
51. A. Bhat, J. M. Amanor-Boadu and A. Guiseppi-Elie, *ACS Sensors*, January 17, 2020, **5**.

52. P. Awasthi, P. Awasthi, R. Mukherjee, R. Mukherjee, S. P. O. Kare, S. P. O. Kare, S. Das and S. Das, *RSC Advances*, 2016/10/26, **6**.
53. *IEEE Sensors Journal*, 2022, **22**.
54. K. ARIYOSHI, Z. SIROMA, A. MINESHIGE, M. TAKENO, T. FUKUTSUKA, T. ABE and S. UCHIDA, *Electrochemistry*, 2022/10/31, **90**.
55. Z. Wang and Z. Wang, *Nature Reviews Clean Technology 2025 1:7*, 2025-05-08, **1**.
56. C. Plank, T. Rüther, L. Jahn, M. Schamel, J. P. Schmidt, F. Ciucci and M. A. Danzer, *Journal of Power Sources*, 2024/02/28, **594**.
57. E. v. Hauff, *The Journal of Physical Chemistry C*, March 28, 2019, **123**.
58. A. HC, N. PQ, G.-M. L, M.-N. E, G. F, C. JJ and D. C, *Nature reviews. Materials*, 2022, **7**.
59. S. NajafiKhoshnoo, T. Kim, J. A. Tavares-Negrete, X. Pei, P. Das, S. W. Lee, J. Rajendran and R. Esfandyarpour, *Advanced Materials Technologies*, 2023/04/01, **8**.
60. P. Dias, S. Javimczik, M. Benevit, H. Veit and A. M. Bernardes, *Waste Management*, 2016/11/01, **57**.
61. V. V. Pinto, M. J. Ferreira, R. Silva, H. A. Santos, F. Silva and C. M. Pereira, *Colloids and Surfaces A: Physicochemical and Engineering Aspects*, 2010/07/20, **364**.
62. P. Hájková, J. Matoušek and P. Antoš, *Applied Catalysis B: Environmental*, 2014/11/01, **160-161**.
63. G. F. Huldin, G. F. Huldin, J. Huang, J. Huang, J. Reitemeier, J. Reitemeier, K. X. Fu and K. X. Fu, *Faraday Discussions*, 2025/02/17, **257**.
64. P. Mostafalu, A. Tamayol, R. Rahimi, M. Ochoa, A. Khalilpour, G. Kiaee, I. K. Yazdi, S. Bagherifard, M. R. Dokmeci, B. Ziaie, S. R. Sonkusale and A. Khademhosseini, *Small*, 2018/08/01, **14**.
65. E. Marin, A. Lanzutti, E. Marin and A. Lanzutti, *Materials 2024, Vol. 17,*, 2023-12-25, **17**.
66. M. Akter, M. T. Sikder, M. M. Rahman, A. K. M. A. Ullah, K. F. B. Hossain, S. Banik, T. Hosokawa, T. Saito and M. Kurasaki, *Journal of Advanced Research*, 2018/01/01, **9**.
67. D. F. Mello, R. Trevisan, N. Rivera, N. K. Geitner, R. T. D. Giulio, M. R. Wiesner, H. Hsu-Kim and J. N. Meyer, *Chemico-Biological Interactions*, 2020/01/05, **315**.
68. M. Ghasemi, T. Turnbull, S. Sebastian, I. Kempson, M. Ghasemi, T. Turnbull, S. Sebastian and I. Kempson, *International Journal of Molecular Sciences 2021, Vol. 22,*, 2021-11-26, **22**.
69. R. E. Smith, R. E. Smith, S. Totti, S. Totti, D. Reid, D. Reid, S. M. Hingley-Wilson, S. M. Hingley-Wilson, E. Velliou, E. Velliou, P. Campagnolo, P. Campagnolo, N. I. Ward, N. I. Ward, J. R. Varcoe, J. R. Varcoe, C. Crean and C. Crean, *Materials Advances*, 2024/03/18, **5**.
70. C. Melios, A. Centeno, A. Zurutuza, V. Panchal, C. E. Giusca, S. Spencer, S. R. P. Silva and O. Kazakova, *Carbon*, 2016/07/01, **103**.
71. T. H. Wan, M. Saccoccio, C. Chen and F. Ciucci, *Electrochimica Acta*, 2015/12/01, **184**.
72. V. Mansfeldova, M. Zlamalova, H. Tarabkova, P. Janda, M. Vorokhta, L. Piliai and L. Kavan, *The Journal of Physical Chemistry C*, January 20, 2021, **125**.
73. S. Kashiwaya, J. Morasch, V. Streibel, T. Toupance, W. Jaegermann, A. Klein, S. Kashiwaya, J. Morasch, V. Streibel, T. Toupance, W. Jaegermann and A. Klein, *Surfaces 2018, Vol. 1, Pages 73-89*, 2018-09-07, **1**.
74. N. Martin, C. Rousselot, D. Rondot, F. Palmino and R. Mercier, *Thin Solid Films*, 1997/05/28, **300**.

75. A. S. Bakri, M. Z. Sahdan, F. Adriyanto, N. A. Raship, N. D. M. Said, S. A. Abdullah and M. S. Rahim, *AIP Conference Proceedings*, 2017/01/03, **1788**.
76. Y. M. Abdulraheem, S. Ghoraishi, L. Arockia-Thai, S. K. Zachariah and M. Ghannam, *Advances in Materials Science and Engineering*, 2013/01/01, **2013**.
77. T. Jia, J. Zhang, J. Wu, D. Wang, Q. Liu, Y. Qi, B. Hu, P. He, W. Pan and X. Qi, *Materials Letters*, 2020/04/15, **265**.
78. D. A. H. Hanaor, C. C. Sorrell, D. A. H. Hanaor and C. C. Sorrell, *Journal of Materials Science 2010 46:4*, 2010-12-08, **46**.
79. D. A. K. Ramadhani, N. Sholeha, N. N. a. Khusna, M. Diantoro, A. N. Afandi, Z. Osman and H. Pujiarti, *Materials Science for Energy Technologies*, 2024/01/01, **7**.
80. M. B. Poudel, C. Yu, H. J. Kim, M. B. Poudel, C. Yu and H. J. Kim, *Catalysts 2020, Vol. 10, Page 546*, 2020-05-14, **10**.
81. Q. Zhang, L. S. Ma, M. H. Shao, J. Z. Huang, M. Ding, X. L. Deng, X. Q. Wei and X. J. Xu, *J Nanomater*, 2014, **2014**.
82. M. A. Alsaiari, N. A. Alhemiary, A. Umar and B. E. Hayden, *Ceram Int*, 2020, **46**, 16310-16320.
83. L. Zhu, L. Zhu, Q. Lu, Q. Lu, L. Lv, L. Lv, Y. Wang, Y. Wang, Y. Hu, Y. Hu, Z. Deng, Z. Deng, Z. Lou, Z. Lou, Y. Hou, Y. Hou, F. Teng and F. Teng, *RSC Advances*, 2017/04/05, **7**.
84. N. Kruse and S. Chenakin, *Applied Catalysis A: General*, 2011/01/04, **391**.
85. G. K. Q. Ganharul, A. Tofanello, A. Bonadio, A. L. M. Freitas, M. T. Escote, A. S. Polo, I. L. Nantes-Cardoso, J. A. Souza, G. K. Q. Ganharul, A. Tofanello, A. Bonadio, A. L. M. Freitas, M. T. Escote, A. S. Polo, I. L. Nantes-Cardoso and J. A. Souza, *Journal of Materials Science 2022 57:36*, 2022-09-22, **57**.
86. D. Depla and D. Depla, *Coatings 2022, Vol. 12, Page 1915*, 2022-12-07, **12**.
87. M. Saghafi, S. Chinnathambi and S. G. Lemay, *Current Opinion in Colloid & Interface Science*, 2023/02/01, **63**.
88. A. Hankin, A. Hankin, F. E. Bedoya-Lora, F. E. Bedoya-Lora, J. C. Alexander, J. C. Alexander, A. Regoutz, A. Regoutz, G. H. Kelsall and G. H. Kelsall, *Journal of Materials Chemistry A*, 2019/11/19, **7**.
89. V. M. Arutyunyan and V. M. Arutyunyan, *Soviet Physics Uspekhi*, 1989-06-30, **32**.
90. S. Al-Hilli, M. Willander, S. Al-Hilli and M. Willander, *Sensors 2009, Vol. 9, Pages 7445-7480*, 2009-09-16, **9**.
91. M. Bischoff, N. Y. Kim, J. B. Joo and A. Marchioro, *The Journal of Physical Chemistry Letters*, September 12, 2022, **13**.
92. Y. Li, B. Xia, B. Jiang, Y. Li, B. Xia and B. Jiang, *Journal of Sol-Gel Science and Technology 2018 87:1*, 2018-06-17, **87**.
93. E. Kuźmicz-Mirosław, M. Kuśmierz, K. Terpiłowski, M. Śmietana, M. Barczak and M. Staniszewska, *Materials*, 2022 Jun 9, **15**.
94. A. Borrás, C. López, V. Rico, F. Gracia, A. R. González-Elipe, †, E. Richter, G. Battiston, R. Gerbasi, N. McSporran, G. Sauthier, a. E. György and A. Figuerasǁ, January 9, 2007, DOI: 10.1021/jp065392.
95. K.-Y. Law, February 20, 2014, DOI: 10.1021/jz402762.
96. A. Samadi, M. Xie, J. Li, H. Shon, C. Zheng and S. Zhao, *Chemical Engineering Journal*, 2021/08/15, **418**.
97. M. Beygisangchin, S. A. Rashid, S. Shafie, A. R. Sadrolhosseini, H. N. Lim, M. Beygisangchin, S. Abdul Rashid, S. Shafie, A. R. Sadrolhosseini and H. N. Lim, *Polymers 2021, Vol. 13, Page 2003*, 2021-06-18, **13**.

98. T. Subramaniam, M. B. Fauzi, Y. Lokanathan and J. X. Law, *International Journal of Molecular Sciences*, 2021 Jun 17, **22**.
99. J. H. Shim, J. W. Lim, B. K. Kim, S. J. Park, S. W. Kim and T. H. Choi, *Archives of Plastic Surgery*, 2015 Jan 14, **42**.
100. M. Holman, *Journal of Wound Care*, 2023-08-12, **32**.
101. T. PL, H. AN, d. S. A, S. G, L. B, M. D and R. TW, *Wound repair and regeneration : official publication of the Wound Healing Society [and] the European Tissue Repair Society*, 2015 Jan-Feb, **23**.
102. J. Lv, F. Lai, L. Lin, Y. Lin, Z. Huang and R. Chen, *Applied Surface Science*, 2007/06/30, **253**.
103. M. Beygisangchin, S. A. Rashid, S. Shafie, A. R. Sadrolhosseini and H. N. Lim, *Polymers*, 2021 Jun 18, **13**.
104. V. T. Lukong, K. Ukoba, K. O. Yoro and T. C. Jen, *Heliyon*, 2022/05/01, **8**.
105. S. Saqlain, B. J. Cha, S. Y. Kim, J. Y. Sung, M. C. Choi, H. O. Seo and Y. D. Kim, *Materials Today Communications*, 2021/03/01, **26**.
106. C.-M. Chen, Y.-C. Hsu and S.-J. Cherng, *Journal of Alloys and Compounds*, 2011/01/21, **509**.
107. L. AC and P. MI, *Acs Meas Sci Au*, 03/08/2023, **3**.
108. B. Hirschorn, M. E. Orazem, B. Tribollet, V. Vivier, I. Frateur and M. Musiani, *Electrochimica Acta*, 2010/08/30, **55**.
109. P. Córdoba-Torres, T. J. Mesquita and R. P. Nogueira, *Electrochimica Acta*, 2013/03/01, **92**.

View Article Online
DOI: 10.1039/D5TB02697K

Data availability

The data supporting this article have been included as part of the Supplementary Information.